Scientific Research Publishing

Open Journal of Applied Sciences, 2026, 16(4), 1068-1084
https://www.scirp.org/journal/ojapps
ISSN Online: 2165-3925
ISSN Print: 2165-3917

Non-Stationary Load Extrapolation over Long Horizons Based on a Frequency-Consistent Diffusion Model

Yu Bai, Fei Meng*

Science of Systems, University of Shanghai for Science and Technology, Shanghai, China
Email: *feimeng@usst.edu.cn

How to cite this paper: Bai, Y. and Meng, F. (2026) Non-Stationary Load Extrapolation over Long Horizons Based on a Frequency-Consistent Diffusion Model. *Open Journal of Applied Sciences*, **16**, 1068-1084.
https://doi.org/10.4236/ojapps.2026.164063

Received: March 11, 2026
Accepted: April 4, 2026
Published: April 7, 2026

Abstract

This study proposes a frequency-consistent diffusion model (FCDM) for long-horizon extrapolation of non-stationary bearing load signals. Condition tokens and spectral-consistency constraints are introduced to preserve spectral and fatigue-related characteristics during tenfold extrapolation. The generated signals are evaluated using PSD, band-energy proportion, Range-Mean distribution, and unit pseudo-damage. Compared with DDPM, FCDM better preserves dominant frequencies, harmonic structure, and band-energy allocation. The dominant frequency error is 1.02%, and the mean harmonic error is 0.52%. FCDM also shows smaller band-energy allocation errors across all frequency bands. In addition, it reproduces the bimodal clustering pattern in the Range-Mean distribution more accurately. The unit pseudo-damage is 1.0978 for FCDM and 1.1280 for DDPM. These results indicate that FCDM improves spectral fidelity and fatigue-related consistency in long-sequence load extrapolation.

Keywords

Diffusion Model, Load Extrapolation, Frequency-Consistency

1. Introduction

Engineering load signals support durability analysis because they reflect real service conditions. Long-duration load histories are essential for fatigue-life prediction and reliability assessment. However, long-term field measurements are often costly and difficult to obtain. Limits in test duration, instrumentation, and operating-condition coverage restrict data collection. Therefore, extending short

measurements into representative long histories is practically important [1] [2].

For non-stationary loads, the challenge is preserving time-varying behavior during extension. Yang *et al.* proposed a load-cycle amplitude model for time-domain extrapolation of non-stationary loads [3]. Some work also discusses constraints under multiple non-stationary loads. Wang *et al.* proposed an extrapolation method for coupled non-stationary loads on drill pipes [4]. Time-frequency approaches are also used for spectrum manipulation in durability practice [5] [6].

In durability applications, extrapolated loads should remain meaningful for fatigue evaluation. Wu *et al.* connected load-spectrum extrapolation with fatigue-life prediction under random loading [7]. Frequency content can also influence fatigue response and should be preserved when needed. Sui *et al.* improved and experimentally verified the fatigue response spectrum method [8]. These findings motivate checks beyond amplitude statistics toward spectral consistency.

Meanwhile, many studies use machine learning to link loading histories with fatigue response. Zhang *et al.* used LSTM models for fatigue prediction under non-stationary vibration loading [9]. Zhang *et al.* also proposed an LSTM-CNN framework for multiaxial fatigue analysis [10]. Yang *et al.* developed a deep-learning method for multiaxial fatigue-life prediction [11]. They later introduced self-attention to represent history and temperature effects [12]. Lian *et al.* proposed knowledge-based machine learning for aluminum alloy fatigue prediction [13].

To reduce purely empirical fitting, physics-informed strategies have been explored. Hao *et al.* proposed a physics-informed learning approach for notch fatigue evaluation [14]. Chen *et al.* enhanced fatigue prediction using frequency-domain representations [15]. Zhang *et al.* combined neural networks with symbolic regression to improve interpretability [16]. Chen *et al.* applied enhanced PINNs to crack propagation and overload fatigue prediction [17]. Mao *et al.* used physics-enhanced learning for fatigue prediction of cold-expanded holes [18]. Fan proposed a knowledge-transfer model for multiaxial fatigue-life prediction [19]. Liao *et al.* proposed an adaptive physics-informed network for path-dependent multiaxial fatigue [20]. Zhu *et al.* applied deep learning to high-cycle fatigue prediction for titanium alloys [21].

However, most studies still predict life or damage from observed load signals. Fewer studies address generating long load histories for downstream durability analysis [7] [8]. This gap is critical for long-duration extrapolation of non-stationary engineering loads.

Diffusion models provide a generative framework through progressive denoising. Ho *et al.* introduced denoising diffusion probabilistic models for learning complex distributions [22]. Nichol and Dhariwal improved diffusion sample quality and efficiency [23]. Song *et al.* proposed implicit diffusion models that reduce sampling cost [24]. Yang *et al.* surveyed diffusion methods and applications, including sequential modeling [25].

Diffusion has also been adapted to time-series tasks with structured temporal

dynamics. Zhao *et al.* proposed diffusion forecasting guided by temporal dependencies and variable relations [26]. Li *et al.* combined diffusion with long-sequence forecasting frameworks for long horizons [27]. Zhu *et al.* proposed a decoupled diffusion-Transformer for enhanced long-term forecasting [28]. Li *et al.* used self-conditioning diffusion for multivariate anomaly detection and reconstruction [29]. Tian *et al.* generated synthetic EHR time series with diffusion, supporting realistic sequence generation [30]. These studies suggest diffusion can learn complex temporal evolution in long sequences. For load extrapolation, length extension alone is not enough. The generated signal must preserve time-varying characteristics from limited measurements.

Existing studies still have two main limitations. (1) Many load extrapolation methods focus on time-domain extension, but insufficiently control spectral drift and energy redistribution in long generated sequences. (2) Current learning-based studies rarely model non-stationary operating conditions explicitly during generation. This makes it difficult to preserve stage-dependent load patterns, cyclic statistics, and fatigue-related characteristics.

To address these issues, this study proposes a Frequency-Consistent Diffusion Model (FCDM). (1) A PSD-based spectral consistency constraint is incorporated into diffusion generation to preserve frequency-domain structure during long-term extrapolation. (2) A condition-token-guided diffusion mechanism is designed to model non-stationary conditions and maintain stage-dependent cyclic and fatigue-related characteristics.

2. Methods

A frequency-consistency-driven conditional diffusion framework is proposed for extrapolating elastic-support force signals during heavy-vehicle cornering. The objective is to generate waveforms that preserve fatigue-relevant spectral statistics. These statistics include dominant peak locations, overall PSD shape, and band-wise energy distribution within a sensitive frequency range. Model training uses sliding-window segmentation of a single long record into fixed-length segments. Pronounced non-stationarity is addressed through unsupervised operating-condition tokens. Tokens are obtained by clustering window-level statistical and spectral descriptors. Temporal smoothing yields piecewise quasi-stationary token sequences. The tokens condition a 1D U-Net diffusion denoiser through feature-wise affine modulation. Training follows a cosine noise schedule and the standard noise-prediction objective. Frequency-consistency regularization is applied to the reconstructed clean signal. This regularization aligns dominant peaks, spectral shape, and band-energy proportions. Long-horizon extrapolation uses DDIM sampling and overlap consistency is enforced between adjacent generated segments. The overlap signal is forward-diffused and injected at each reverse step. This constraint reduces boundary artifacts and improves sequence coherence. The specific process is shown in **Figure 1**.

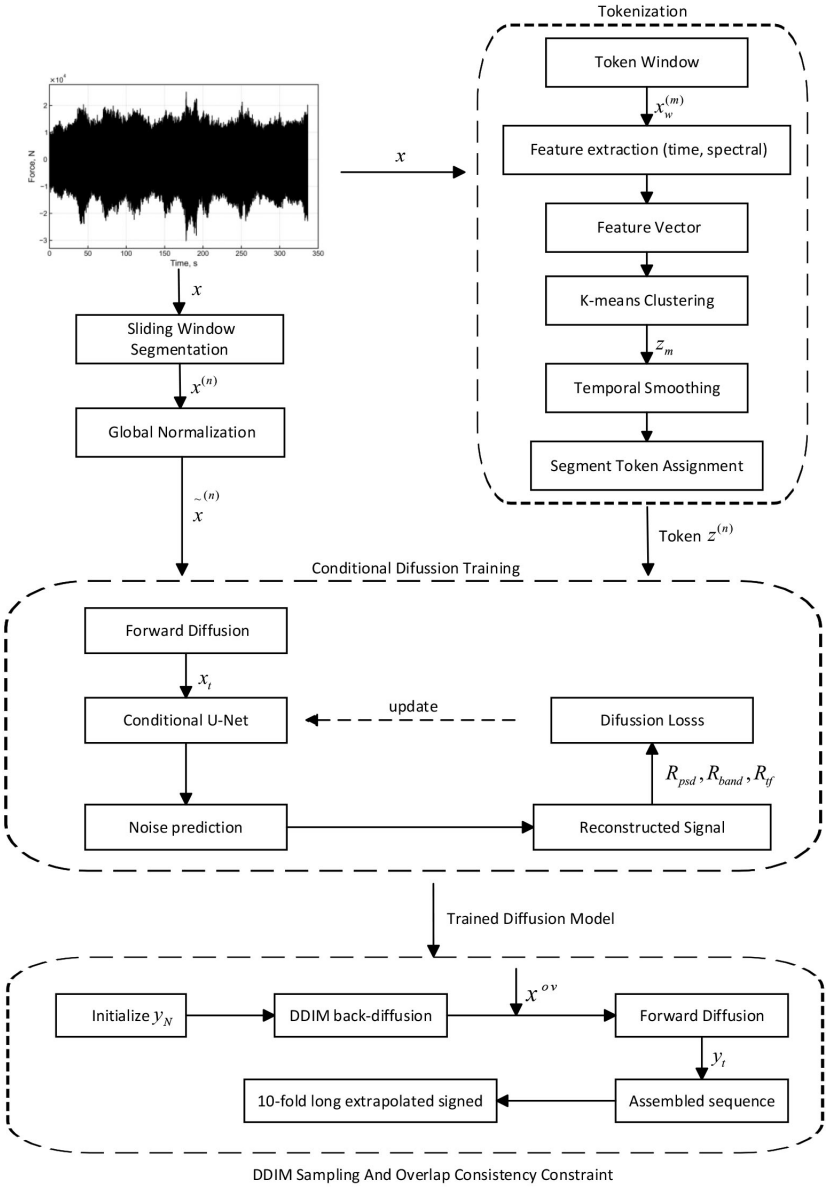

Figure 1. FCDM model.

2.1. Data Preparation and Segment Sampling

Let $\mathrm{x} \in \mathbb{R}^T$ denote the discrete-time force record sampled at f_s. Training segments are obtained by sliding-window sampling:

$$\mathrm{x}^{(n)} = \left[x_{s_n}, x_{s_n+1}, \cdots, x_{s_n+L-1} \right]^\top \in \mathbb{R}^L,$$

where L is the segment length and H is the hop size, so $s_n = 1 + (n-1)H$. Global normalization is applied:

$$\tilde{\mathrm{x}}^{(n)} = \frac{\mathrm{x}^{(n)} - \mu}{\sigma},$$

where μ and σ are computed from the full record. In the present study, the model is trained in a self-supervised generative manner on sliding-window seg-

ments extracted from this single record, rather than on separately split training and test records. Therefore, the reported results should be interpreted as an evaluation of long-horizon statistical extrapolation on a single measured record, rather than as a benchmark of cross-record predictive generalization.

The input signal used in this step corresponds to the reconstructed continuous load-time history obtained after filtering, rainflow-based cycle screening, and interpolation, as described in Section 3.

2.2. Operating-Condition Tokenization for Nonstationary Loads

Cornering loads typically exhibit pronounced nonstationary characteristics. To address this issue, a discrete operating-condition tokenization strategy is introduced to provide piecewise quasi-stationary conditioning for the generative model. For the m-th token window $x_w^{(m)}$, a descriptor vector $f^{(m)} \in \mathbb{R}^{d_{dis}}$ is constructed as

$$f^{(m)} = \left[\psi_{time}\left(x_w^{(m)}\right), \psi_{peak}\left(x_w^{(m)}\right), \psi_{spec}\left(x_w^{(m)}\right) \right].$$

Token windows are extracted with a window length of 3.0 s and a hop of 0.5 s. In the present implementation, the descriptor dimension is 15, including six time-domain statistics (mean, standard deviation, RMS, peak-to-peak value, skewness, and kurtosis), seven normalized narrow-band energy ratios centered at the dominant frequencies identified from the Welch PSD, and two spectral descriptors, namely the spectral centroid and spectral bandwidth.

After feature standardization, K-means clustering is employed to assign a discrete operating-condition token $z_m \in \{1, \cdots, K\}$. In this study, $K = 5$ is used. The raw token sequence is then temporally smoothed by majority voting within a 5.0 s window. To suppress short-lived fluctuations, token segments with durations shorter than 3.0 s are merged into the longer adjacent segment, resulting in a piecewise-constant token timeline $z(\tau)$.

Each training segment $\tilde{x}^{(n)}$, centered at time τ_n, is then assigned a token

$$z^{(n)} = z(\tau_n),$$

which serves as the conditioning variable for the diffusion denoiser during training. The choice $K = 5$ reflects a practical compromise between preserving stage-dependent condition differences and avoiding excessive token fragmentation.

For conditioning, each generated segment is assigned an operating-condition token. Since future condition labels are not available, the token assignment during rollout follows a cyclic mapping over the token timeline estimated from the measured signal. Specifically, the center time of each generated segment is mapped to a virtual time on the original signal using a modulo operation, and the corresponding token is assigned based on the nearest token label.

2.3. Conditional Diffusion Model

A diffusion process with N steps is adopted. The forward diffusion process is defined as

$$q\left(x_t \mid x_{t-1}\right)=\mathcal{N}\left(\sqrt{1-\beta_t}\, x_{t-1}, \beta_t I\right), t=1, \cdots, N.$$

This process admits the closed-form representation

$$x_t=\sqrt{\bar{\alpha}_t}\, x_0+\sqrt{1-\bar{\alpha}_t}\, \epsilon, \epsilon \sim \mathcal{N}(0, I),$$

where

$$\alpha_t=1-\beta_t, \bar{\alpha}_t=\prod_{i=1}^{t} \alpha_i.$$

A cosine noise schedule is adopted for $\left\{\beta_t\right\}$. The denoising network $\epsilon_\theta\left(x_t, t, z\right)$ is parameterized using a 1D U-Net architecture. Let e_t denote the embedding of the diffusion step and e_z the embedding of the operating-condition token. Their sum

$$e=e_t+e_z$$

is used to condition intermediate feature maps h through feature-wise affine modulation:

$$\operatorname{Mod}(h ; e)=\gamma(e) \odot h+\beta(e).$$

2.4. Frequency-Consistency Regularization

To encourage the generated signals to preserve fatigue-relevant spectral characteristics, a frequency-consistency regularization term is introduced. This regularization emphasizes spectral structure within a sensitive frequency band $\left[f_{\min }, f_{\max }\right]$.

2.4.1. Dominant Frequencies and Peak-Centered Weighting

The dominant frequencies $\left\{f_p\right\}_{p=1}^{P}$ are extracted from the Welch PSD of the training record within the band $\left[f_{\min }, f_{\max }\right]$. Let $\left\{f_k\right\}_{k=1}^{K_f}$ denote the discrete frequency samples within this interval.

A peak-centered Gaussian weighting function is defined as

$$w_k \equiv w\left(f_k\right)=\sum_{p=1}^{P} \exp\left(-\frac{\left(f_k-f_p\right)^2}{2 \sigma_f^2}\right), k=1, \cdots, K_f.$$

The weights w_k are normalized over $k=1, \cdots, K_f$ to ensure scale stability.

2.4.2. Peak-Aware Weighted Log-PSD Discrepancy

Let $S_x(f)$ and $S_{\hat{x}}(f)$ denote the Welch PSD estimates of the ground-truth signal x_0 and the reconstructed clean signal $\hat{x}_0$, respectively. The peak-aware spectral discrepancy is defined as

$$R_{psd}=\frac{\sum_{k=1}^{K_f} w_k\left|\log\left(S_{\hat{x}}\left(f_k\right)+\varepsilon\right)-\log\left(S_x\left(f_k\right)+\varepsilon\right)\right|}{\sum_{k=1}^{K_f} w_k+\varepsilon}.$$

2.4.3. Band-Energy Proportion Alignment

Let $\left\{B_b\right\}_{b=1}^{B}$ denote a partition of the frequency band $\left[f_{\min }, f_{\max }\right]$. The band-en-

ergy proportion is defined as

$$r_b(x) = \frac{\int_{B_b} S_x(f)\mathrm{d}f}{\sum_{j=1}^{B}\int_{B_j} S_x(f)\mathrm{d}f}, b = 1, \cdots, B.$$

Based on this definition, the band-proportion regularizer is formulated as

$$R_{band} = \frac{1}{B}\sum_{b=1}^{B}\left|r_b(\hat{x}_0) - r_b(x_0)\right|.$$

2.4.4. Time-Frequency Migration Consistency

To preserve the temporal evolution of spectral energy, frame-wise band-energy proportions p are computed from STFT magnitudes. The following regularization penalizes discrepancies in both spectral magnitude and temporal variation:

$$R_{tf} = \left\|\hat{p} - p\right\|_1 + \eta\left\|\Delta\hat{p} - \Delta p\right\|_1.$$

2.5. Training Objective: Regularized Diffusion Learning

The standard diffusion objective minimizes the noise prediction error

$$L_{diff} = \mathbb{E}_{t,x_0,\epsilon}\left[\left\|\epsilon - \epsilon_\theta(x_t, t, z)\right\|_2^2\right].$$

Given x_t, the reconstructed clean signal estimate is computed as

$$\hat{x}_0 = \frac{x_t - \sqrt{1-\bar{\alpha}_t}\,\epsilon_\theta(x_t, t, z)}{\sqrt{\bar{\alpha}_t} + \varepsilon}.$$

The model parameters are optimized using the regularized objective

$$\min_\theta L_{diff} + g(t)R_{freq} + R_{stab}.$$

The frequency-consistency regularization term is defined as

$$R_{freq} = \lambda_{psd}R_{psd} + \lambda_{band}R_{band} + \lambda_{tf}R_{tf}.$$

The gating function $g(t)$ reduces the influence of spectral regularization during high-noise diffusion steps. The stabilization term R_{stab} includes auxiliary components such as log-scale RMS alignment, multi-resolution STFT consistency, and a floor-suppression mechanism with narrow exclusions around the dominant frequencies $\{f_p\}$. These terms improve numerical robustness and stabilize the training process.

2.6. Inference: DDIM Sampling with Overlap-Constrained Consistency

In this study, long-horizon extrapolation is defined as generating a load signal with a duration significantly longer than that of the available measured sequence. Let the source signal have a duration of T_s, and the target signal have a duration of T_t. In our experiments, we consider a tenfold extrapolation, *i.e.*, $T_t \approx 10T_s$.

The generation is performed in a segment-wise manner. Each segment has a length of $L = 3.0$ s, with an overlap of $L_o = 0.5$ s between adjacent segments. At each rollout step, the model generates one segment, and only the non-overlap-

ping portion of length $L - L_o = 2.5$ s is appended. The number of rollout steps N is determined by the desired target duration:

$$N \approx \frac{T_t - L}{L - L_o}.$$

To accelerate sampling, deterministic diffusion implicit models (DDIM) are employed during inference. For stability, the reconstructed clean estimate is clipped element-wise in the normalized domain:

$$\hat{x}_0 = \text{clip}\left(\hat{x}_0, -c, c\right).$$

Long-horizon extrapolation is achieved by sequentially generating segments while enforcing consistency within an overlap region. Let $y \in \mathbb{R}^L$ denote the segment to be generated, and L_o the overlap length. Define the overlap index set

$$\Omega = \{1, \cdots, L_o\}$$

and its complement

$$\bar{\Omega} = \{L_o + 1, \cdots, L\}.$$

Let $x^{ov} \in \mathbb{R}^{L_o}$ denote the most recently generated suffix that must be matched in the overlap region.

At diffusion step t, let y_t denote the current latent variable. The overlap constraint is enforced by replacing the overlap portion with a forward-diffused version of x^{ov}. Specifically,

$$y_t^{ov} \sim q\left(x^{ov}, t\right),$$

and the constrained latent variable is defined as

$$\left[y_t\right]_\Omega = y_t^{ov}, \left[y_t\right]_{\bar{\Omega}} = \left[y_t\right]_{\bar{\Omega}}.$$

Equivalently, using a binary mask $m \in \{0,1\}^L$ defined as $m_i = 1$ for $i \in \Omega$ and $m_i = 0$ otherwise, the same operation can be written as

$$y_t = (1 - m) \odot y_t + m \odot \tilde{y}_t,$$

where $\tilde{y}_t$ is a length-L vector whose first L_o entries equal y_t^{ov} and whose remaining entries are zeros.

After the reverse diffusion process is completed, only the non-overlap portion $y_{\bar{\Omega}}$ is appended to the generated sequence. This overlap-constrained sampling strategy effectively reduces boundary artifacts and improves temporal coherence under large extrapolation factors. The specific parameters can be seen in Table 1.

Table 1. Parameter setting.

Group	Parameter	Value
Data	f_s	2000 Hz
Segments	L, H	3.0 s, 0.25 s
Tokens	L_w, H_w, K	3.0 s, 0.5 s, 5

Continued

Diffusion	N	1000
Spectral	P, σ_f	7, 3.8 Hz
Regularization	$\lambda_{psd}, \lambda_{band}$	0.13, 0.60
Inference	DDIM steps, L_o, c	800, 0.5 s, 8

3. Experimental Data

Experimental data is collected from the elastic support force of a heavy-duty vehicle during cornering conditions. The raw measurement contains high-frequency noise due to vibration and sensor effects. Therefore, a low-pass filter with a cutoff frequency of 500 Hz is first applied to obtain a denoised load signal.

To further focus on fatigue-relevant load components, rainflow counting is performed on the filtered signal to identify load cycles. Cycles with amplitudes lower than 10% of the maximum load are discarded. This threshold is introduced to remove very small-amplitude cycles that are dominated by measurement noise and contribute negligibly to fatigue damage, especially under a high damage exponent.

After cycle screening, a continuous load-time history is reconstructed using linear interpolation between the retained turning points. As a result, the dominant spectral structure and fatigue-relevant characteristics (e.g., cycle amplitude distribution and pseudo-damage) are largely preserved. The reconstructed signal is then used as the final input for model training and evaluation.

The reconstructed signal is shown in Figure 2.

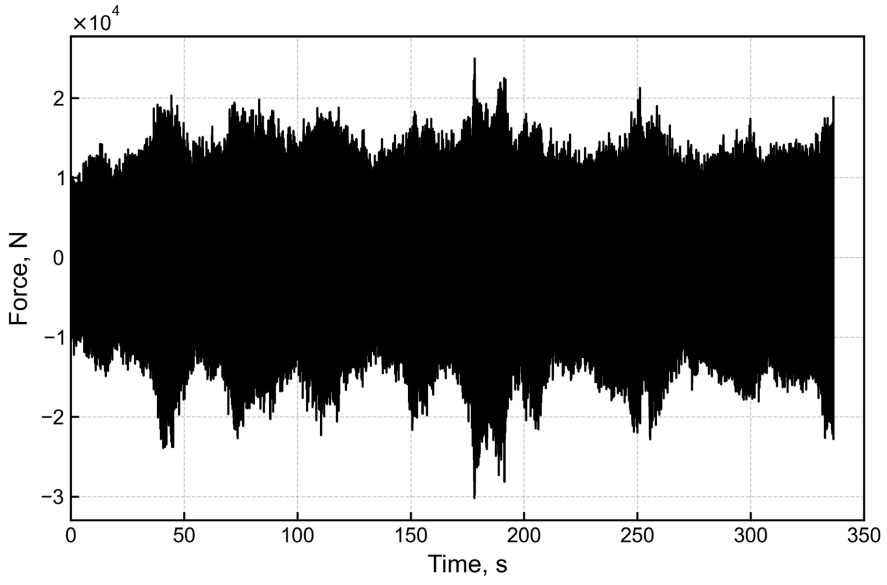

Figure 2. Load time-domain signal.

Figure 2 indicates pronounced amplitude modulation and clear stage-dependent fluctuations. Local bursts and intermittent spikes are superimposed on broad-

band oscillations. The signal therefore exhibits piecewise quasi-stationary behavior with overall non-stationarity. This implies time-varying statistics and spectral-energy migration across different phases.

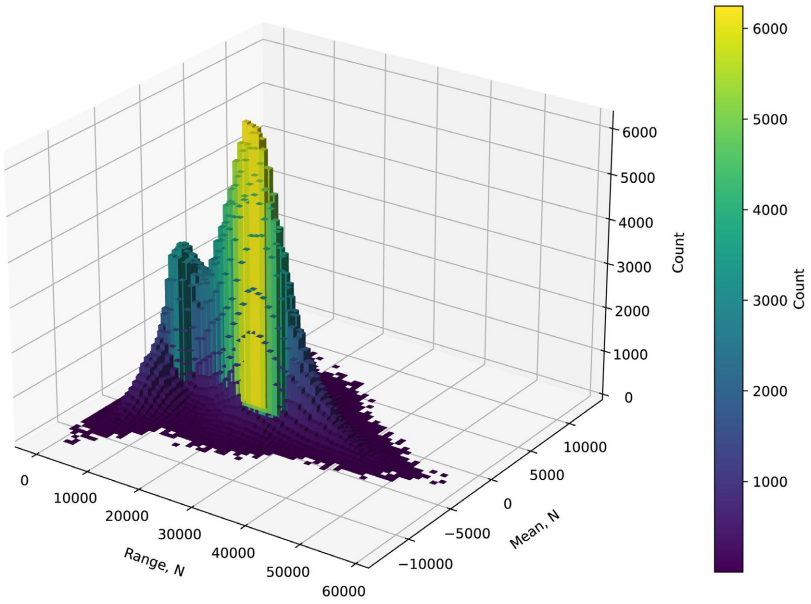

Figure 3. Rainflow 3D distribution.

The rainflow 3D distribution in Figure 3 reveals concentrated ridges in the range-mean plane. These ridges suggest dominant cycle groups under specific operating phases. A sparse high-range tail remains, indicating rare but potentially damage-critical cycles. The distribution is multimodal and skewed, reflecting nonstationary cornering loads. These properties motivate the use of FCDM with operating-condition tokens and frequency-consistency constraints.

4. Experimental Results

This section evaluates FCDM from three aspects: spectral structure preservation, band-energy distribution, and fatigue-related statistical consistency. First, PSD is used to assess whether the generated signal preserves the dominant frequencies and harmonic structure of the real load. Then, band-energy proportion is introduced to compare how different methods distribute spectral energy across key frequency bands. Finally, Range-Mean distributions and unit pseudo-damage are used to examine fatigue-related characteristics. Since the objective of this study is long-horizon extrapolation of engineering loads rather than pointwise time-domain reconstruction, the discussion focuses on spectral fidelity and fatigue relevance.

4.1. PSD Comparison

Figure 4 compares the PSDs of the real signal and the FCDM-generated signal over 0 - 500 Hz. FCDM reproduces the main spectral structure with good fidelity. The dominant peaks appear at nearly the same frequencies, and the overall spec-

tral envelope is well preserved. This indicates that the proposed spectral-consistency constraint effectively suppresses peak drift and spectral distortion during extrapolation.

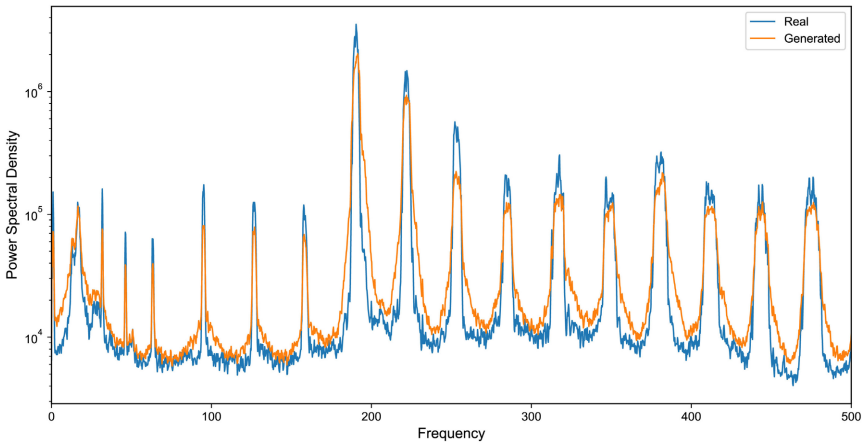

Figure 4. PSD comparison between real signal and FCDM.

The dominant frequency error is 1.02%, and the mean harmonic error is 0.52%, showing that FCDM accurately captures both the principal excitation frequencies and their harmonic components. The JS divergence is 0.103 in the PSD domain and 0.039 in the time domain, which indicates good agreement in both spectral and statistical terms.

4.2. Pseudo-Damage-Based Accuracy Evaluation

To ensure a fair comparison, the DDPM baseline uses the same network backbone, diffusion-step setting, optimizer, batch size, and training epochs as the proposed FCDM. The same clipping strategy and overlap-constrained DDIM sampling procedure are also applied during inference.

The only differences are that DDPM does not incorporate operating-condition tokens and does not include the frequency-consistency regularization terms. Therefore, the performance differences can be attributed to the proposed conditioning mechanism and frequency-domain constraints.

PSD curves provide a direct visual comparison, but they do not fully reveal how spectral energy is distributed across bands. Therefore, band-energy proportion was further analyzed. The bands were not uniformly spaced. Instead, the 0 - 500 Hz range was first partitioned according to equalized Welch PSD integrals and then adjusted around dominant peaks. This strategy preserves both global energy distribution and local spectral sensitivity. The final bands were 0 - 180 Hz, 180 - 191 Hz, 191 - 222 Hz, 222 - 256 Hz, 256 - 380 Hz, and 380 - 500 Hz.

Figure 5 compares the band-energy proportions of the real signal, FCDM, and DDPM. FCDM is consistently closer to the real signal, whereas DDPM shows larger deviations in several bands. This indicates that the spectral-consistency constraint improves the preservation of energy allocation across frequency bands.

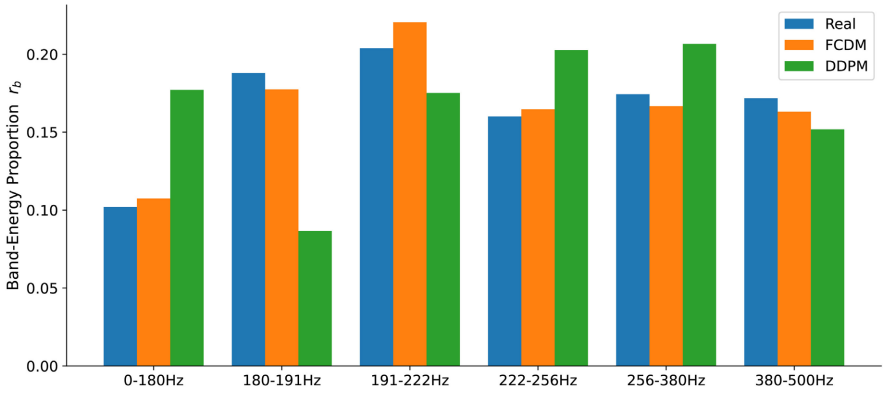

Figure 5. Band-energy proportion comparison among Real, FCDM and DDPM.

FCDM shows small errors in all bands, with absolute deviations generally below 0.02. DDPM shows much larger deviations, especially in the 180 - 191 Hz band, where strong underestimation is observed (see **Table 2**). Additional discrepancies appear in the 0 - 180 Hz, 222 - 256 Hz, and 256 - 380 Hz bands. These results suggest that, without explicit spectral constraints, the pure diffusion model tends to redistribute energy across bands.

Table 2. Band-energy proportion errors.

Band (Hz)	0 - 180	181 - 191	191 - 222	222 - 256	256 - 380	380 - 500
FCDM	0.54%	−1.06%	1.67%	0.46%	−0.76%	−0.85%
DDPM	7.52%	−10.13%	−2.87%	4.25%	3.23%	−1.99%

FCDM shows a slight over-allocation in the 191 - 222 Hz band and slight under-allocation in the 180 - 191 Hz and 256 - 500 Hz ranges. This indicates a mild concentration of energy around the dominant band. Even so, its deviation remains much smaller than that of DDPM.

Although a full ablation study is not included in the present work, the contributions of different components can be interpreted based on the comparison results and the design of the method. The operating-condition tokens provide coarse-grained conditioning that helps capture nonstationary behavior, while the frequency-consistency regularization terms (PSD consistency, band-energy consistency, and time-frequency consistency) directly constrain the generated signal in the spectral domain.

The observed improvements over DDPM, particularly in band-energy allocation and pseudo-damage, suggest that both the conditional tokens and the frequency-domain constraints contribute to enhanced statistical fidelity.

4.3. Fatigue-Related Statistical Characteristics

To quantify fatigue-related consistency, a rainflow-based pseudo-damage metric is introduced. Let R_i denote the cycle range in the i-th rainflow bin and n_i

the corresponding cycle count. The pseudo-damage is defined as

$$D = \sum_i n_i R_i^m,$$

where m is the damage exponent. In this study, $m = 8$ is adopted to emphasize the contribution of large-amplitude cycles.

Since the extrapolated sequences are significantly longer than the original measured signal, a direct comparison of accumulated pseudo-damage is not meaningful due to the difference in duration. To address this issue, a normalized metric, referred to as unit pseudo-damage, is introduced. Specifically, the pseudo-damage of each signal is normalized by that of the real reference signal over a comparable duration, so that the real signal has a unit value of 1. Values greater than 1 indicate overestimation of fatigue severity, while values closer to 1 indicate better agreement with the measured signal.

PSD curves provide a direct visual comparison, but they do not fully reveal how spectral energy is distributed across bands.

Spectral consistency alone does not guarantee fatigue relevance. The statistical characteristics of load cycles must also be examined.

Figure 6 compares the Range-Mean distributions of the real signal and the FCDM-generated signal. The two distributions exhibit a similar bimodal structure, with high-density regions located at nearly the same positions. In addition, the concentration and spread of the clustered regions are well preserved, indicating that FCDM captures not only the dominant cycle locations but also the overall distribution pattern of fatigue-related load cycles. This agreement suggests that the generated signal remains statistically consistent with the real load in the cycle domain.

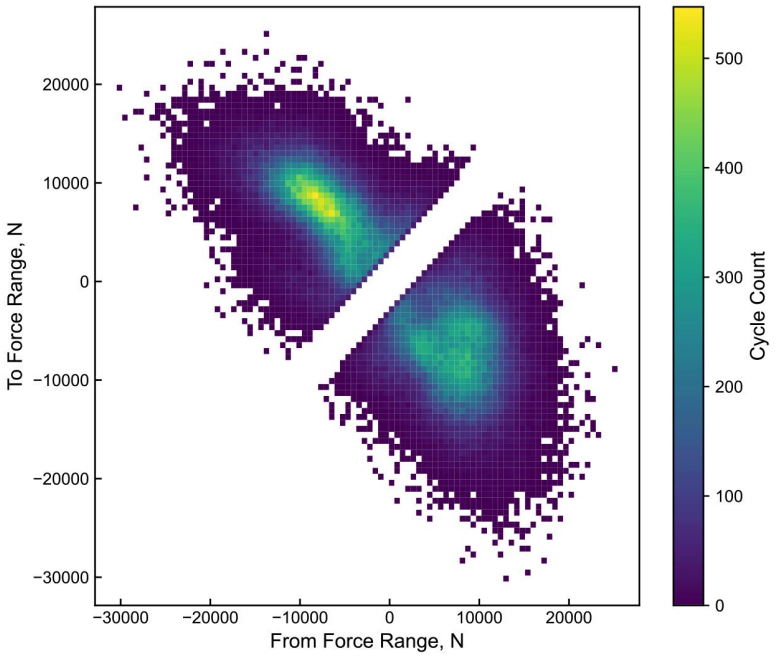

(1) Rainflow from-to matrix of real

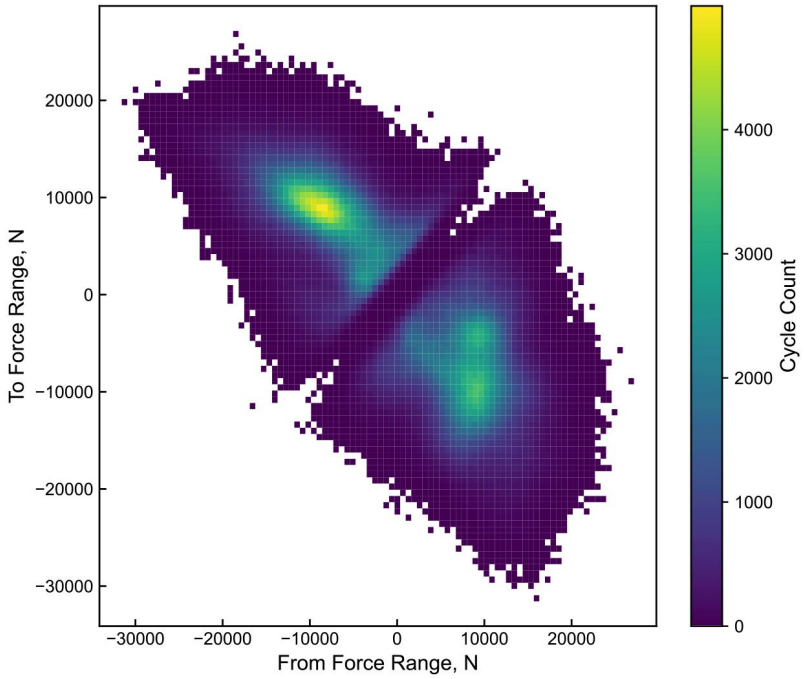

(2) Rainflow from-to matrix of FCDM

Figure 6. Rainflow from-to matrix comparison.

Table 3 summarizes the unit pseudo-damage and cycle count. The unit pseudo-damage of FCDM is 1.0978, corresponding to a deviation of 9.78% from the real signal, whereas DDPM gives 1.1280, with a deviation of 12.80%. Both methods remain reasonably close to the real load in terms of overall fatigue severity, but FCDM is more accurate. Combined with the band-energy results, this indicates that improved spectral consistency leads to more reliable fatigue-related statistical characteristics.

Table 3. Unit pseudo-damage and range count (m = 8).

Methods	Count	Unit pseudo-damage
Real	104042	1
DDPM	1107074	1.128
FCDM	1020649	1.098

5. Conclusions

This study proposed a frequency-consistent diffusion model for long-horizon extrapolation of non-stationary bearing load signals under turning conditions. The method integrates condition tokens with spectral-consistency constraints to improve frequency-domain fidelity during generation. Unlike conventional diffusion models, the proposed framework explicitly preserves dominant frequencies, harmonic structure, and band-energy allocation.

The results demonstrate that FCDM reproduces the main spectral characteris-

tics of the measured load with high accuracy. The PSD comparison shows that the dominant peaks and overall spectral envelope are well maintained. Band-energy analysis further confirms that FCDM yields smaller deviations than DDPM across all key frequency bands. This indicates that spectral constraints effectively suppress undesired energy redistribution during long-duration extrapolation. Fatigue-related evaluation provides additional support for the proposed method. The generated signals preserve the bimodal Range-Mean distribution observed in the measured load.

Moreover, FCDM achieves a lower pseudo-damage error than DDPM, indicating better consistency in fatigue-relevant statistical behavior. Overall, the proposed method improves both spectral fidelity and engineering relevance of extrapolated load signals.

These findings suggest that FCDM is a promising approach for long-sequence load generation in fatigue-oriented applications. Future work will focus on improving local peak amplitude recovery and extending the framework to broader operating conditions.

Conflicts of Interest

The authors declare no conflicts of interest regarding the publication of this paper.

References

[1] Cheng, X., Han, T., Yang, P. and Zhang, X. (2021) Compilation of Load Spectrum for 5MN Metal Extruder Based on Long Short-Term Memory Network. *Applied Sciences*, **11**, Article 9708. https://doi.org/10.3390/app11209708

[2] Dai, D., Chen, D., Wang, S., Li, S., Mao, X., Zhang, B., *et al.* (2023) Compilation and Extrapolation of Load Spectrum of Tractor Ground Vibration Load Based on CEEMDAN-POT Model. *Agriculture*, **13**, Article 125. https://doi.org/10.3390/agriculture13010125

[3] Yang, Z., Liu, X., Song, Z. and Liu, H. (2024) The Load Cycle Amplitude Model: An Efficient Time-Domain Extrapolation Technique for Non-Stationary Loads in Agricultural Machinery. *Agriculture*, **14**, Article 2322. https://doi.org/10.3390/agriculture14122322

[4] Wang, H., Zhang, Z., Zhang, J., Shen, Y. and Wang, J. (2024) A Novel Load Extrapolation Method for Multiple Non-Stationary Loads on the Drill Pipe of a Rotary Rig. *Machines*, **12**, Article 75. https://doi.org/10.3390/machines12010075

[5] Yang, Y., Zhang, Z., Peng, L., Jin, J. and Wang, Q. (2023) Accelerated Editing Method for Vehicle Durability Fatigue Load Spectrum Based on Wigner-Ville Transform. *Sensors*, **23**, Article 6435. https://doi.org/10.3390/s23146435

[6] Liu, X., Tan, J. and Long, S. (2024) Multi-Axis Fatigue Load Spectrum Editing for Automotive Components Using Generalized S-Transform. *International Journal of Fatigue*, **188**, Article 108503. https://doi.org/10.1016/j.ijfatigue.2024.108503

[7] Wu, Q., Zhao, Y. and Liu, X. (2024) Fatigue Life Prediction of Metal Materials under Random Loads Based on Load Spectrum Extrapolation. *International Journal of Fatigue*, **187**, Article 108473. https://doi.org/10.1016/j.ijfatigue.2024.108473

[8] Sui, G., Jin, X., Cui, H. and Zhang, Y. (2024) Improvement and Test Verification of

the Fatigue Response Spectrum Method. *Mechanical Systems and Signal Processing*, **217**, Article 111519. https://doi.org/10.1016/j.ymssp.2024.111519

[9] Zhang, C., Wan, R., He, J., Yu, J. and Zhao, Y. (2024) Non-Stationary Vibration Fatigue Life Prediction of Automotive Components Based on Long Short-Term Memory Network. *International Journal of Fatigue*, **187**, Article 108459. https://doi.org/10.1016/j.ijfatigue.2024.108459

[10] Zhang, C., Wan, R., He, J. and Yu, J. (2025) A Multiaxial Fatigue Life Analysis Method for Automotive Components Based on LSTM-CNN. *International Journal of Fatigue*, **199**, Article 109062. https://doi.org/10.1016/j.ijfatigue.2025.109062

[11] Yang, J., Kang, G., Liu, Y. and Kan, Q. (2021) A Novel Method of Multiaxial Fatigue Life Prediction Based on Deep Learning. *International Journal of Fatigue*, **151**, Article 106356. https://doi.org/10.1016/j.ijfatigue.2021.106356

[12] Yang, J., Kang, G. and Kan, Q. (2022) A Novel Deep Learning Approach of Multiaxial Fatigue Life-Prediction with a Self-Attention Mechanism Characterizing the Effects of Loading History and Varying Temperature. *International Journal of Fatigue*, **162**, 106851. https://doi.org/10.1016/j.ijfatigue.2022.106851

[13] Lian, Z., Li, M. and Lu, W. (2022) Fatigue Life Prediction of Aluminum Alloy via Knowledge-Based Machine Learning. *International Journal of Fatigue*, **157**, Article 106716. https://doi.org/10.1016/j.ijfatigue.2021.106716

[14] Hao, W.Q., Tan, L., Yang, X.G., Shi, D.Q., Wang, M.L., Miao, G.L., *et al.* (2023) A Physics-Informed Machine Learning Approach for Notch Fatigue Evaluation of Alloys Used in Aerospace. *International Journal of Fatigue*, **170**, Article 107536. https://doi.org/10.1016/j.ijfatigue.2023.107536

[15] Chen, S., Zhou, X. and Bai, Y. (2025) A Frequency Domain Enhanced Multi-View Neural Network Approach to Multiaxial Fatigue Life Prediction for Various Metal Materials. *International Journal of Fatigue*, **190**, Article 108620. https://doi.org/10.1016/j.ijfatigue.2024.108620

[16] Zhang, P., Tang, K., Wang, A., Wu, H. and Zhong, Z. (2024) Neural Network Integrated with Symbolic Regression for Multiaxial Fatigue Life Prediction. *International Journal of Fatigue*, **188**, Article 108535. https://doi.org/10.1016/j.ijfatigue.2024.108535

[17] Chen, Z., Dai, Y. and Liu, Y. (2024) Crack Propagation Simulation and Overload Fatigue Life Prediction via Enhanced Physics-Informed Neural Networks. *International Journal of Fatigue*, **186**, Article 108382. https://doi.org/10.1016/j.ijfatigue.2024.108382

[18] Mao, J., Xian, Z., Wang, X., Hu, D., Pan, J., Wang, R., *et al.* (2025) Fatigue Life Prediction of Cold Expansion Hole Using Physics-Enhanced Data-Driven Method. *International Journal of Fatigue*, **190**, Article 108634. https://doi.org/10.1016/j.ijfatigue.2024.108634

[19] Gan, L., Fan, Z., Wu, H. and Zhong, Z. (2025) Prediction of Multiaxial Fatigue Life with a Data-Driven Knowledge Transfer Model. *International Journal of Fatigue*, **190**, Article 108636. https://doi.org/10.1016/j.ijfatigue.2024.108636

[20] Liao, H., Pan, J., Su, X., Sun, X. and Chen, X. (2025) A Path-Dependent Adaptive Physics-Informed Neural Network for Multiaxial Fatigue Life Prediction. *International Journal of Fatigue*, **193**, Article 108799. https://doi.org/10.1016/j.ijfatigue.2024.108799

[21] Zhu, S., Zhang, Y., Zhu, B., Zhang, J., He, Y. and Xu, W. (2024) High Cycle Fatigue Life Prediction of Titanium Alloys Based on a Novel Deep Learning Approach. *International Journal of Fatigue*, **182**, Article 108206. https://doi.org/10.1016/j.ijfatigue.2024.108206

[22] Ho, J., Jain, A. and Abbeel, P. (2020) Denoising Diffusion Probabilistic Models. *Advances in Neural Information Processing Systems*, **33**, 1-12. https://proceedings.neurips.cc/paper/2020/hash/4c5bcfec8584af0d967f1ab10179ca4b-Abstract.html

[23] Nichol, A.Q. and Dhariwal, P. (2021) Improved Denoising Diffusion Probabilistic Models. *Proceedings of the* 38*th International Conference on Machine Learning*, **139**, 8162-8171. https://proceedings.mlr.press/v139/nichol21a.html

[24] Song, J., Meng, C. and Ermon, S. (2021) Denoising Diffusion Implicit Models. *International Conference on Learning Representations*, Online, 3-7 May 2021, 1-20 https://openreview.net/forum?id=St1giarCHLP

[25] Yang, L., Zhang, Z., Song, Y., Hong, S., Xu, R., Zhao, Y., *et al.* (2023) Diffusion Models: A Comprehensive Survey of Methods and Applications. *ACM Computing Surveys*, **56**, 1-39. https://doi.org/10.1145/3626235

[26] Zhao, T., Song, G., Li, X., Cui, L. and Zhang, C. (2024) Diff-MGR: Dynamic Causal Graph Attention and Pattern Reproduction Guided Diffusion Model for Multivariate Time Series Probabilistic Forecasting. *Information Sciences*, **675**, Article 120742. https://doi.org/10.1016/j.ins.2024.120742

[27] Li, J., Chen, W., Liu, Y., Yang, J., Zhou, Z. and Zeng, D. (2026) Diffinformer: Diffusion Informer Model for Long Sequence Time-Series Forecasting. *Expert Systems with Applications*, **299**, Article 129944. https://doi.org/10.1016/j.eswa.2025.129944

[28] Zhu, J., Liu, D., Chen, H., Liu, J. and Tao, Z. (2025) Dtsformer: Decoupled Temporal-Spatial Diffusion Transformer for Enhanced Long-Term Time Series Forecasting. *Knowledge-Based Systems*, **309**, Article 112828. https://doi.org/10.1016/j.knosys.2024.112828

[29] Li, Y., Wen, Z., Chen, Z., Mei, J., Lin, M. and Zhu, M. (2025) Diffusion Models with Self-Conditioning Guidance for Multivariate Time Series Anomaly Detection. *Knowledge-Based Systems*, **330**, Article 114511. https://doi.org/10.1016/j.knosys.2025.114511

[30] Tian, M., Chen, B., Guo, A., Jiang, S. and Zhang, A.R. (2024) Reliable Generation of Privacy-Preserving Synthetic Electronic Health Record Time Series via Diffusion Models. *Journal of the American Medical Informatics Association*, **31**, 2529-2539. https://doi.org/10.1093/jamia/ocae229